

Type-II Lateral Heterostructures of Monolayer Halide Double Perovskites for Optoelectronic Applications

Hongxia Zhong, Mao Yang, Gang Tang,* and Shengjun Yuan*



Cite This: *ACS Energy Lett.* 2020, 5, 2275–2282



Read Online

ACCESS |



Metrics & More

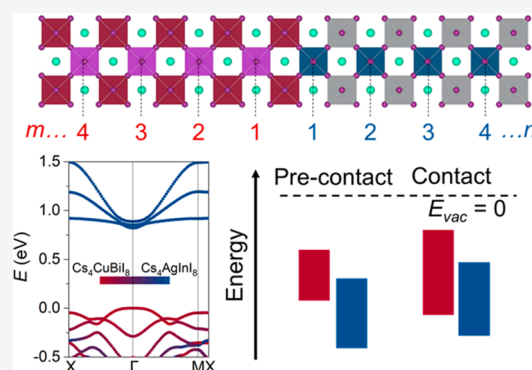


Article Recommendations



Supporting Information

ABSTRACT: Recently, layered halide double perovskites ($A_4M^I M^III X_8$) have attracted growing interest and provided a wide range of basic building blocks for fabricating vertical and lateral heterostructures (LHs). Here, we take Cs_4AgInI_8 and Cs_4CuBiI_8 as the representative compounds of monolayer double perovskites to design suitable LHs for optoelectronic applications using first-principles calculations. Our results reveal that the constructed $(Cs_4CuBiI_8)_3/(Cs_4AgInI_8)_3$ LH could possess the desired direct band gap and type-II band alignment. The electronic properties such as band gap and effective mass can be further tuned by applying strain or adjusting components. More importantly, we find that the transition dipole moments between the band edges can be modulated effectively by tensile strain and components, providing new insights for the rational utilization of double perovskites that possess partially forbidden transitions for optoelectronic devices. Our studies propose stable atomic structures for optoelectronic devices based on double perovskite LHs with desired electronic and optical properties.



Lead (Pb) halide perovskites that include three-dimensional (3D) (e.g., $CH_3NH_3PbI_3$) and layered two-dimensional (2D) structures (e.g., $(C_4H_9NH_3)_2PbI_4$) have recently attracted considerable attention because of their successful applications in photovoltaic devices.^{1–7} In addition to solar cells, they have also been widely exploited in other optoelectronic fields, such as light-emitting diodes,³ lasers,⁸ and photodetectors.⁵ However, despite the superior performance of Pb halide perovskite-based devices, the toxicity of Pb has become an increasing concern for their commercialization.⁹

An efficient method to solve this problem is to replace two Pb(II) with a couple of B(I)/B(III) cations to form halide double perovskites $A_2B(I)B(III)X_6$ (A = monovalent cation; B(I) = Ag^+ , Cu^+ ; B(III) = Sb^{3+} , Bi^{3+} , In^{3+} ; X = halogen).^{7,9–14} However, most of the reported double perovskites have wide indirect band gaps (>1.9 eV) and large carrier effective masses due to the mismatch in angular momentum of the frontier atomic orbitals,¹⁴ and the synthesized $Cs_2AgInCl_6$ with direct band gap has been proven to show inversion symmetry-induced parity-forbidden transitions.⁹ The relatively large band gap and parity-forbidden transition in halide double perovskite are not desired for ideal photovoltaic applications. One way to modify the electronic and optical properties of double perovskites is to form their layered counterparts,^{15–19} such

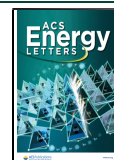
as $(C_4H_9NH_3)_4AgBiBr_8$, $PA_4AgInCl_8$ (PA = propylammonium), $[AE2T]_2AgBiI_8$ (AE2T = 5,5'-diylbis(aminoethyl)-[2,2'-bithiophene]), and $(CAA)_4CuBiI_8$ (CAA = cyclohexylamine). Indeed, some layered double perovskites are reported to exhibit potential optoelectronic properties with direct band gaps¹⁵ and can be used as basic building blocks for novel heterojunction devices, similar to the conventional 2D materials.

Recently, van der Waals (vertical) heterostructure devices based on halide perovskites/2D materials (e.g., $CH_3NH_3PbI_3/WSe_2$) and halide perovskites/halide perovskites (e.g., $(n-CH_3(CH_2)_3NH_3)_2PbI_4/(n-CH_3(CH_2)_3NH_3)_2(CH_3NH_3)Pb_2I_7$) have been demonstrated to show promising optoelectronic performances such as high photoresponsivity and good rectification behavior.^{20–23} However, there are difficulties in controlling the stacking orientation and sample size, as those revealed in 2D materials.^{24,25} On the other hand, lateral heterostructures (LHs) with atomically clean and sharp

Received: May 14, 2020

Accepted: June 2, 2020

Published: June 2, 2020



interfaces have been introduced,^{24,26} and their electronic and optical properties are different from their counterparts formed in vertical heterostructures. These reports are mainly experimental contributions,^{23,27–30} and a first fabrication of various lateral heterostructures and superlattices of 2D halide perovskites by the solution-phase sequential growth has been reported very recently.³⁰ To our knowledge, theoretical studies on the LHs of halide perovskites are still absent in the literature.

In this work, we take $\text{Cs}_4\text{AgInI}_8$ and $\text{Cs}_4\text{CuBiI}_8$ as the representative compounds of monolayer double perovskites to study their LHs based on first-principles calculations. We focus mainly on the properties related to their optoelectronic applications and try to provide valuable guidance for their experimental realizations. We will find out how the electronic properties, such as the band gap and band alignment, are modulated by the atomic structures in $(\text{Cs}_4\text{CuBiI}_8)_m/(\text{Cs}_4\text{AgInI}_8)_n$ (where m and n are integers) LHs. Importantly, we find that the direct band gap appears only in the case of $m \geq 3$, and the type-II band alignment can be found in other LHs formed by Cu-VA and Ag-IIIa double perovskites. The effects of strain and modification of block size in perovskites will be studied. In particular, the transition dipole moments between the band edges which are highly related to optoelectronic applications will be investigated. We finally study the mechanical properties of LHs, including the Young's modulus and Poisson's ratios. Our studies will provide guidance for experimentally achieving double perovskite LHs with tunable optoelectronic properties in the future.

Figure 1a shows the crystal structure of layered near Dion–Jacobson type halide double perovskites $\text{A}_4\text{B(I)B(III)X}_8$,³¹ formed by the incorporation of organic spacer cations A^+ into 3D double perovskites. In terms of specific electron configuration, the B^+ cations in $\text{A}_4\text{B(I)B(III)X}_8$ can be classified into three classes: (i) the group IA elements (Na^+ , K^+ , Rb^+ , and Cs^+) that have empty s and d outermost orbitals, (ii) the group IB elements (Cu^+ , Ag^+ , and Au^+) that have empty s but full d outermost orbitals, and (iii) the group IIIA elements (In^+ and Tl^+) that have full s outermost orbitals. The B^{3+} cations can be divided into two categories: (i) the group IIIA elements (In^{3+} and Tl^{3+}) that have empty s orbitals, (ii) the group VA elements (Sb^{3+} and Bi^{3+}) that have full s outermost orbitals. According to recent theoretical and experimental studies,^{10,11,32} Na^+ -based double perovskites are electronically zero-dimensional (0D) because of the $[\text{NaX}_6]$ octahedra, which do not contribute to the conduction band minimum (CBM) and valence band maximum (VBM). In^+ - and Tl^+ -based double perovskites are thermodynamically unstable and toxic, respectively. Therefore, only the group IB elements are highly desired for B^+ cations. Here we focus only on the study of double perovskites consisting of the group IB elements and IIIA elements or the group IB elements and VA elements.

Because the electronic structure of halide perovskites is mainly determined by $[\text{BX}_6]$ inorganic networks, while A-site organic cations have only an indirect effect on electronic states around the Fermi level by distorting the inorganic networks,^{15,33} we thus use Cs atom to replace the A-site long-chain organic molecule (e.g., $\text{C}_4\text{H}_9\text{NH}_3$) in this work to reduce the computational cost. On the basis of the above consideration, here, we select monolayer $\text{Cs}_4\text{AgInI}_8$ and $\text{Cs}_4\text{CuBiI}_8$ (see Figure 1b,c) as the representative compounds to design halide double perovskite LHs for optoelectronic

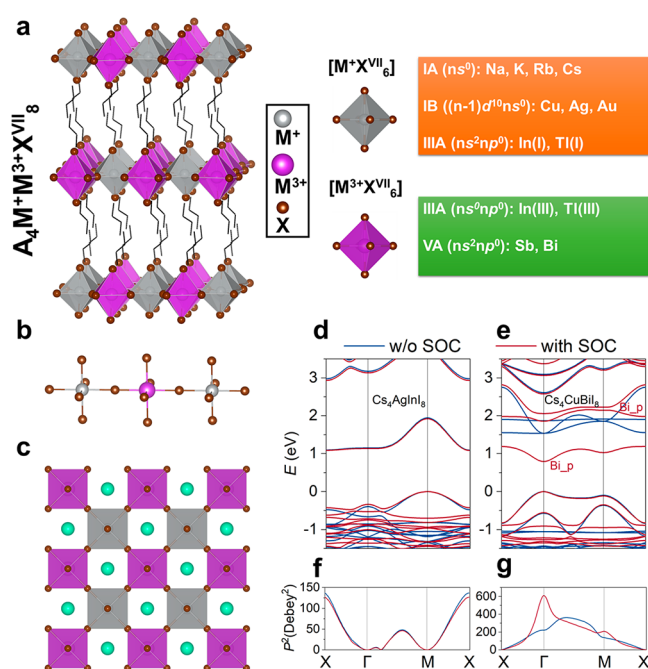


Figure 1. (a) Illustration of metal cation choice strategy to design layered Pb-free halide double perovskites. Side (b) and top (c) views of atomic configurations of undistorted monolayer $\text{A}_4\text{B(I)–B(III)X}_8$. The green spheres in panel c represent Cs atoms, which disappear in panel b for clarity. Band structures (d and e) and corresponding square of transition dipole moments between the top valence band and the bottom conduction band (f and g) for monolayer $\text{Cs}_4\text{AgInI}_8$ (d and f) and $\text{Cs}_4\text{CuBiI}_8$ (e and g) without (with) SOC included, respectively. The valence band maximum is set to zero.

applications. The calculated lattice constant for monolayer $\text{Cs}_4\text{AgInI}_8$ ($\text{Cs}_4\text{CuBiI}_8$) is 8.30 (8.37) Å (see Table 1), which is much smaller than the value of 11.96 (10.37) Å in its corresponding undistorted bulk phase.^{34,35} On the other hand, the lattice constant of monolayer $\text{Cs}_4\text{AgInI}_8$ ($\text{Cs}_4\text{CuBiI}_8$) is comparable to that of monolayer $\text{Cs}_4\text{AgBiBr}_8$ (8.16 Å).¹⁵ Among B(I)–I and B(III)–I bond lengths (see Table S1), the Bi–I bond length is the largest, and the Cu–I bond length is the smallest.

First, we calculate the band structures of monolayer $\text{Cs}_4\text{AgInI}_8$ and $\text{Cs}_4\text{CuBiI}_8$ along high-symmetry direction in the first Brillouin zone, as shown in Figure 1d,e. Unlike the direct band gap of bulk $\text{Cs}_2\text{AgInCl}_6$,¹⁵ for monolayer $\text{Cs}_4\text{AgInI}_8$, the VBM is at the M point, while CBM is at the X point, indicating an indirect band gap of 1.09 eV by the Perdew, Burke, and Ernzerhof (PBE) method (the band structure calculated by other method can be found in Figure S1). The predicted electron and hole effective masses are 2.01 ($X\text{–}\Gamma$) and 0.65 ($M\text{–}X$) m_0 , respectively (see Table 1). The large electron effective mass results from the flat lowest conduction band along the $X\text{–}\Gamma$ direction. The calculated squares of the dipole transition matrix elements,^{9,36} P^2 , at Γ and M points are zero in Figure 1f, indicating forbidden transitions. These parity-forbidden transitions also appear in the bulk $\text{Cs}_2\text{AgInCl}_6$,⁹ not an ideal condition for solar cell applications. However, monolayer $\text{Cs}_4\text{CuBiI}_8$ shows the desired direct band gap of 1.54 eV by PBE method, with both VBM and CBM located at the Γ point. This is different from the indirect band gap of bulk $\text{Cs}_2\text{CuBiBr}_6$.³⁵ The direct–

Table 1. Calculated Effective Mass, Band Gap, and Lattice Constants for Monolayer $\text{Cs}_4\text{AgInI}_8$, $\text{Cs}_4\text{CuBiI}_8$, and Their Related Lateral Heterostructures^a

| | effective mass (m_0) | | | | band gap (eV) | a (Å) | b (Å) |
|---|--------------------------|---------------------|-------------|---------------------|---------------|---------|---------|
| | electron | | hole | | | | |
| | Γ -X | Γ -M | Γ -X | Γ -M | | | |
| $\text{Cs}_4\text{AgInI}_8$ | 0.24 (X-M) | 2.01 (X- Γ) | 0.65 (M-X) | 0.84 (M- Γ) | 1.09 (1.09) | 8.30 | 8.30 |
| $\text{Cs}_4\text{CuBiI}_8$ | 0.24 | 0.26 | 0.27 | 0.30 | 1.54 (0.79) | 8.37 | 8.37 |
| $(\text{Cs}_4\text{CuBiI}_8)_3/(\text{Cs}_4\text{AgInI}_8)_3$ | 0.33 | 0.38 | 6.24 | 7.63 | 0.81 (0.81) | 50.02 | 8.33 |
| $(\text{Cs}_4\text{CuBiI}_8)_4/(\text{Cs}_4\text{AgInI}_8)_2$ | 0.52 | 0.55 | 0.90 | 0.95 | 0.79 | 50.12 | 8.35 |
| $(\text{Cs}_4\text{CuBiI}_8)_5/(\text{Cs}_4\text{AgInI}_8)_1$ | 0.95 | 0.92 | 0.76 | 0.82 | 0.82 | 50.22 | 8.36 |
| $(\text{Cs}_4\text{CuBiI}_8)_4/(\text{Cs}_4\text{AgInI}_8)_4$ | 0.36 | 0.35 | 0.45 | 0.51 | 0.78 | 66.72 | 8.34 |

^aThe band directions for effective masses are given in parentheses for monolayer $\text{Cs}_4\text{AgInI}_8$. We also list the band gap calculated by the PBE+SOC method in parentheses for comparison.

indirect (indirect–direct) band gap transition for Ag–In (Cu–Bi) double perovskite is attributed to the reduction in dimensionality, which has been observed in Ag–Bi systems.¹⁵ The dispersive valence band along the band edges give a small hole effective mass of 0.27 (0.30) m_0 along Γ -X (Γ -M) in Table 1. Moreover, $\text{Cs}_4\text{CuBiI}_8$ exhibits allowed and strong transitions between band edges. Further, we investigate the effect of spin–orbit coupling (SOC) on the band structures. It is shown that the inclusion of SOC does not modify the band edges of $\text{Cs}_4\text{AgInI}_8$ (see Figure 1d) but induces a lower conduction band and reduces the band gap to 0.79 eV in $\text{Cs}_4\text{CuBiI}_8$ (see Figure 1e). The strong SOC effects associated with the heavy Bi atom also appear in other halide double perovskites containing Bi atoms.¹⁵ The induced lower conduction band is rather dispersive, giving rise to small electron effective mass of 0.24 (0.26) m_0 along Γ -X (Γ -M) in Table 1. In addition, the SOC effect does not change the forbidden or allowed transition characteristics (see Figure 1f,g).

To combine the advantages of two materials into a single system to achieve new physics, we construct a series of lateral heterostructures using monolayer $\text{Cs}_4\text{CuBiI}_8$ and $\text{Cs}_4\text{AgInI}_8$, i.e. $(\text{Cs}_4\text{CuBiI}_8)_m/(\text{Cs}_4\text{AgInI}_8)_n$, where m and n indicate the number of different building blocks, as shown in Figure 2a. Similar to the square lattice of monolayer sample, $(\text{Cs}_4\text{CuBiI}_8)_m/(\text{Cs}_4\text{AgInI}_8)_n$ LHs also own an ideal square lattice from the top view of the atomic configurations, with the stitched direction along the x axis. According to previous studies,^{25,37} the building block size has significant effects on the electronic properties of the stitched lateral heterostructures. Thus, we compare the band structures of $(\text{Cs}_4\text{CuBiI}_8)_m/(\text{Cs}_4\text{AgInI}_8)_n$ LHs in Figure S2 and find that there is a transition from indirect ($m \leq 2$) to direct ($m \geq 3$) band gap in the lateral heterostructures. The gap value decreases monotonically from 1.00 to 0.78 eV with increasing block width m and changes a little from $m = 3$ to 4. This direct-gap feature would be preferred for optoelectronics and photocatalysis.³⁸ Therefore, we take $(\text{Cs}_4\text{CuBiI}_8)_3/(\text{Cs}_4\text{AgInI}_8)_3$ as a case for the following discussions.

We first examine the stability of the considered $(\text{Cs}_4\text{CuBiI}_8)_3/(\text{Cs}_4\text{AgInI}_8)_3$ LH. The calculated binding energy is 13 meV, indicating that the LH can be stable.³⁷ Then, we present the projected band structure of $(\text{Cs}_4\text{CuBiI}_8)_3/(\text{Cs}_4\text{AgInI}_8)_3$ LH in Figure 2b. It is shown that $(\text{Cs}_4\text{CuBiI}_8)_3/(\text{Cs}_4\text{AgInI}_8)_3$ is a direct-gap semiconductor, with a band gap (0.81 eV) located at the Γ point. The direct-gap feature is totally different from the indirect gap of

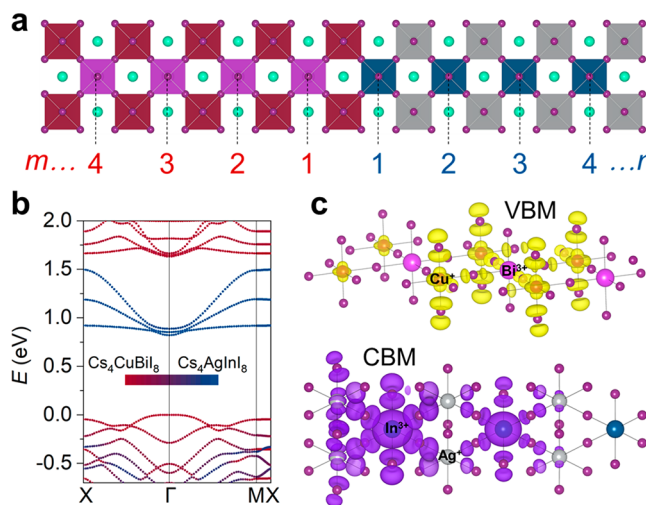


Figure 2. (a) Top view of atomic configurations of $(\text{Cs}_4\text{CuBiI}_8)_m/(\text{Cs}_4\text{AgInI}_8)_n$ LHs. (b) Projected band structure of $(\text{Cs}_4\text{CuBiI}_8)_3/(\text{Cs}_4\text{AgInI}_8)_3$ LH. The valence band maximum is set to zero. Band-decomposed charge density for (c) VBM and CBM of $(\text{Cs}_4\text{CuBiI}_8)_3/(\text{Cs}_4\text{AgInI}_8)_3$ LH.

pristine monolayer $\text{Cs}_4\text{AgInI}_8$ in Figure 1d. However, the less dispersive VBM demonstrates a heavy hole effective mass of 7.63 m_0 (Table 1), much larger than the hole effective mass of 0.30 (0.84) m_0 in pristine $\text{Cs}_4\text{CuBiI}_8$ ($\text{Cs}_4\text{AgInI}_8$) monolayers. On the other hand, we can see that the VBM and CBM of $(\text{Cs}_4\text{CuBiI}_8)_3/(\text{Cs}_4\text{AgInI}_8)_3$ LH are contributed by $\text{Cs}_4\text{CuBiI}_8$ and $\text{Cs}_4\text{AgInI}_8$, respectively, demonstrating the desired type-II heterostructure. Interestingly, we note that $[\text{Cu}_4\text{Cl}]^{3+}$ and $[\text{InCl}_6]^{3-}$ clusters also align in a type-II arrangement in experimentally synthesized $\text{Cs}_3\text{Cu}_4\text{In}_2\text{Cl}_{13}$ structure.³⁹ The separate distributions are more clearly in band-decomposed charge density for VBM and CBM in Figure 2c. The VBM is dominated by Cu d_{z^2} orbitals, while CBM mainly consists of In s orbitals, accompanied by I p orbitals. On the basis of the orbital analysis, we can infer that Cu-VA and Ag-IIIA double perovskite could form type-II heterostructures, such as $(\text{Cs}_4\text{CuBiI}_8)_3/(\text{Cs}_4\text{AgTlI}_8)_3$ and $(\text{Cs}_4\text{CuSbI}_8)_3/(\text{Cs}_4\text{InInI}_8)_3$ LHs in Figure S3. Moreover, we note that the $(\text{Cs}_4\text{AgBiI}_8)_1/(\text{Cs}_4\text{InInI}_8)_1$ LH forms type-I band alignment in Figure S4, with the dispersive band edges all dominated by a $\text{Cs}_4\text{InInI}_8$ component,^{13,40,41} which could be very interesting in some special solar electronic applications. We also use the PBE+SOC method to calculate the band structure of $(\text{Cs}_4\text{CuBiI}_8)_3/(\text{Cs}_4\text{AgInI}_8)_3$ LH in Figure S5. It can be seen

that SOC does not alter the direct band edge dispersion and type-II band alignment. This is because the Bi-dominated states are far from the band edges in the projected density of states in Figures S6 and S7. For type-II lateral heterostructures, the photon-generated electrons and holes are confined at opposite components, thereby decreasing the recombination rate and facilitating the quantum efficiency. Thus, the type-II band alignment of $(\text{Cs}_4\text{CuBiI}_8)_3/(\text{Cs}_4\text{AgInI}_8)_3$ LH has potential applications in optoelectronic devices.

In order to analyze the charge transfer in the type-II $(\text{Cs}_4\text{CuBiI}_8)_3/(\text{Cs}_4\text{AgInI}_8)_3$ LH, we plot plane-averaged charge density difference $\Delta\rho(x)$ along the stitched direction (x -axis) in Figure 3a. Here, a positive $\Delta\rho(x)$ indicates the electron

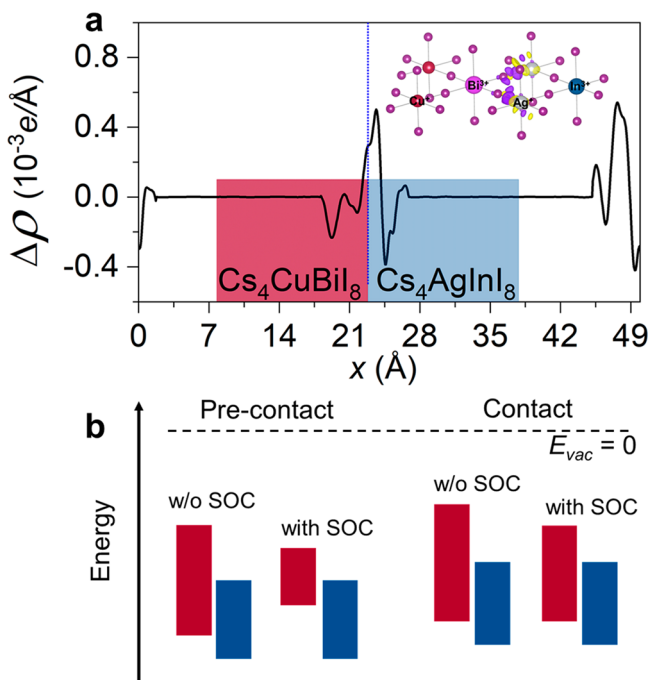


Figure 3. (a) Plane-averaged charge density difference $\Delta\rho(x)$ of $(\text{Cs}_4\text{CuBiI}_8)_3/(\text{Cs}_4\text{AgInI}_8)_3$ LH. The inset shows a three-dimensional charge density difference, and the isosurface value is $2 \times 10^{-3} \text{ e}/\text{\AA}^3$. The purple and yellow areas represent electron accumulation and depletion, respectively. (b) Schematic energy level diagrams of $(\text{Cs}_4\text{CuBiI}_8)_3/(\text{Cs}_4\text{AgInI}_8)_3$ LH in the precontact and contact states without and with SOC effects. The top and bottom of the rectangles represent the values of VBM and CBM. The red and blue rectangles represent the energy levels of $\text{Cs}_4\text{CuBiI}_8$ and $\text{Cs}_4\text{AgInI}_8$, respectively.

accumulating at this point, while a negative value means the depletions of electrons. Our results show that the plane-averaged density is zero when x is far enough from the heterostructure interface, while near the interface, charge redistribution occurs, and few electrons ($\sim 10^{-3}e$) flow from $\text{Cs}_4\text{CuBiI}_8$ to $\text{Cs}_4\text{AgInI}_8$. This is more evident in the 3D charge density difference plotted in the insets, which clearly presents the electron accumulating in the $\text{Cs}_4\text{AgInI}_8$ region. Furthermore, the charge-transfer path agrees with the band edge analysis of type-II $(\text{Cs}_4\text{CuBiI}_8)_3/(\text{Cs}_4\text{AgInI}_8)_3$ LH. Meanwhile, no significant charge transfer suggests chemical bonds between the building blocks, different from the weak van der Waals forces in vertical heterostructures. The chemical bonds can be further verified by electron localization functions (ELFs) of the bonds in the lateral heterostructures in Figure S8, where

bonding type across the interface is very similar to the cases of pristine $\text{Cs}_4\text{CuBiI}_8$ and $\text{Cs}_4\text{AgInI}_8$ monolayers. Because of the charge transfer and chemical bonds at the interface, the seamless $(\text{Cs}_4\text{CuBiI}_8)_3/(\text{Cs}_4\text{AgInI}_8)_3$ LH is potentially used for optoelectronic transport devices.

Energy level shift is another important parameter to describe the interfacial characteristics of heterostructures. We thus plot the energy levels of monolayer $\text{Cs}_4\text{CuBiI}_8$ and $\text{Cs}_4\text{AgInI}_8$ in the precontact and contact states without and with SOC effects in Figure 3b. The energy levels are aligned with the vacuum level (E_{vac}), and E_{vac} is set to zero. In the precontact state, the values of CBM and VBM in $\text{Cs}_4\text{CuBiI}_8$ are higher than those of $\text{Cs}_4\text{AgInI}_8$. When they contact with each other, the electrons spontaneously move from $\text{Cs}_4\text{CuBiI}_8$ to $\text{Cs}_4\text{AgInI}_8$, and the holes flow in the opposite direction. Therefore, the electrons accumulate in the $\text{Cs}_4\text{AgInI}_8$ interface and the holes accumulate in the $\text{Cs}_4\text{CuBiI}_8$ side, leading to the decrease (increase) of interface electric potential in the $\text{Cs}_4\text{CuBiI}_8$ ($\text{Cs}_4\text{AgInI}_8$). This confirms again the charge-transfer path in Figure 3a. In terms of dynamics, the electron flow is driven by the work function, defined as the energy difference between the vacuum level and the Fermi level. The calculated work functions of $\text{Cs}_4\text{CuBiI}_8$ and $\text{Cs}_4\text{AgInI}_8$ are 4.30 and 4.51 eV, respectively. In the contact state, the Fermi level of $\text{Cs}_4\text{CuBiI}_8$ will be pulled down and the Fermi level of $\text{Cs}_4\text{AgInI}_8$ will be pushed up until the Fermi levels are at the same energy. The energy level diagram of $(\text{Cs}_4\text{CuBiI}_8)_3/(\text{Cs}_4\text{AgInI}_8)_3$ LH is thus type-II level arrangement, which is consistent with previous projected band structure analysis. With the inclusion of SOC effects, the conduction band offset is reduced, but the type-II level arrangement does not change for $(\text{Cs}_4\text{CuBiI}_8)_3/(\text{Cs}_4\text{AgInI}_8)_3$ LH.

Apart from the direct gap nature and interfacial characteristics, a large transition dipole matrix element (P^2) between band edges for constructed LHs is also highly desirable for optoelectronic applications. Because the optical absorption of a semiconductor is fundamentally determined by the transition matrix and the joint density of states (JDOS),⁴² we calculate P^2 for $(\text{Cs}_4\text{CuBiI}_8)_3/(\text{Cs}_4\text{AgInI}_8)_3$ LH as shown in Figure S9 and find that P^2 is zero between VBM and CBM. This indicates the partially forbidden transitions between band edges in $(\text{Cs}_4\text{CuBiI}_8)_3/(\text{Cs}_4\text{AgInI}_8)_3$. In addition to the heavy hole effective mass and partially forbidden transitions, the above discussions reveal that the constructed $(\text{Cs}_4\text{CuBiI}_8)_3/(\text{Cs}_4\text{AgInI}_8)_3$ LH exhibits potential optoelectronic applications. In the following discussion, we will continue the search for effective strategies for further improvements of these two issues.

Applying strain is a simple and powerful way to modify the electronic properties of semiconductors.^{43,44} We further explore the electronic structures of $(\text{Cs}_4\text{CuBiI}_8)_3/(\text{Cs}_4\text{AgInI}_8)_3$ LH under external biaxial strains from -4% to 4% in Figure 4a. With the increasing of the strain, the position of CBM is driven continuously to shift away from the Fermi level, resulting in a broadening of the band gap. The band gap of $(\text{Cs}_4\text{CuBiI}_8)_3/(\text{Cs}_4\text{AgInI}_8)_3$ LH increases by 45.5%, from 0.66 to 0.96 eV, while the top of the valence band position is retained. Thus, the strain is an effective way to modulate the band gap close to the suitable value of 1.5 eV for solar cells. To explore the origin of the band variation tendency of the CBM as the applied biaxial strains, we present its charge density under different biaxial strains in the insets. It is shown that the CBM is dominated by In s orbitals for compressive strain, while it is

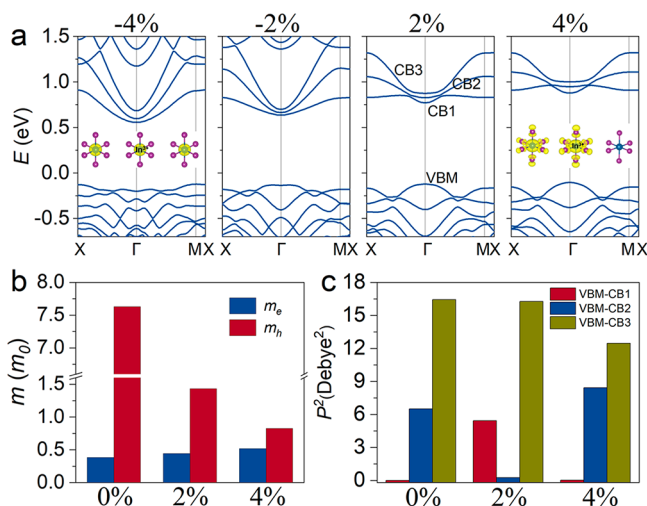


Figure 4. (a) Band structures of the $(\text{Cs}_4\text{CuBiI}_8)_3/(\text{Cs}_4\text{AgInI}_8)_3$ LH for biaxial strains from -4% to 4% . All bands are shifted to align the deep Cs $5s$ states. The insets show charge density for CBM of the strained $(\text{Cs}_4\text{CuBiI}_8)_3/(\text{Cs}_4\text{AgInI}_8)_3$ LH, and the isosurface value is $1.5 \times 10^{-3} \text{ e}/\text{\AA}^3$. Three conduction band states at Γ point have been labeled. (b) Electron and hole effective masses (in units of m_0), and (c) transition dipole matrix element between VBM and different conduction bands at Γ point for unstrained and strained $(\text{Cs}_4\text{CuBiI}_8)_3/(\text{Cs}_4\text{AgInI}_8)_3$ LH.

contributed by In s and I p orbitals for other cases, and the In–I s – p orbital hybridizations are weakened by the biaxial strain, leading to an increase of the energy of CBM and a larger band gap. When we apply a uniaxial strain along the x or y direction, the change of the band structures follows a similar tendency as the one observed in biaxial strains. In fact, the variation of the band structure in a biaxial strain is a superimposition of two individual uniaxial strains, and the strain along the y direction plays the dominant role in determining the band gap.

On the other hand, although the direct band nature is retained for tensile strain (positive strain), the band gap becomes indirect for compressive strain (negative strain). As an indirect band gap is unfavored for solar cell applications, in the following we will focus only on the cases with direct band gaps. We summarize the electron and hole effective masses and transition dipole matrix elements between VBM and labeled conduction bands for the tensile strain cases in Figure 4b,c. The heavy hole effective mass is reduced by an order of magnitude, from 6.24 (7.63) m_0 to 0.77 (0.83) m_0 along Γ -X (Γ -M). Compared with the change of hole effective mass with the tensile strain, the electron effective mass nearly does not depend on the strain, increasing from 0.33 (0.38) m_0 to 0.48 (0.52) m_0 along Γ -X (Γ -M). Therefore, the strain is an effective way to tune the band gap and carrier effective mass at the same time. Besides the increased band gap and reduced carrier effective mass, more interesting, the strain can also tune the transition dipole matrix elements in Figure 4c. For unstrained $(\text{Cs}_4\text{CuBiI}_8)_3/(\text{Cs}_4\text{AgInI}_8)_3$ LH, the transition between CB1 and VBM states is partially forbidden, but the transitions from CB2 and CB3 to VBM are allowed with a considerable P^2 value (6 – 17 D^2) at Γ point. As the photon excited electrons in the conduction bands follow the Fermi–Dirac distribution, at room temperature ($k_B T = 26 \text{ meV}$), the electron populations occupied at the labeled three states (CB1 to CB3 in Figure 4a) can be estimated and listed in Table S3. It is shown that most of the photon-generated electrons are at

CB1 states in the thermal equilibrium situation, and the lifetime of the photon-generated carriers at CBM (CB1) is quite long, as a result of the forbidden transition between CB1 and VBM. Furthermore, with 2% strain, the transition between VBM and CBM is allowed ($P^2 = 5.62 \text{ D}^2$), while the transition between VBM and CB2 is partially forbidden. Thus, applying a strain can control the electron lifetime and recombination rate, which are very useful for certain electronic designs.⁴⁵

Besides strain, adjusting components is another way to tune the optoelectronic properties of lateral heterostructures. We then emphasize the $(\text{Cs}_4\text{CuBiI}_8)_m/(\text{Cs}_4\text{AgInI}_8)_n$ LHs with different ratios of components, which may further possess certain guiding significance for the subsequent experimental work. Here, we propose a series of consecutive $(\text{Cs}_4\text{CuBiI}_8)_m/(\text{Cs}_4\text{AgInI}_8)_n$ with m from 1 to 5 and keep structure width constant ($m + n = 6$). The corresponding band structures are illustrated in Figure 5. The type-II band alignment and

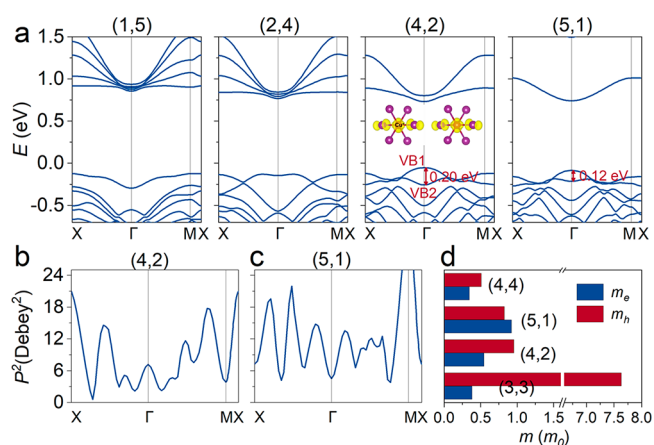


Figure 5. (a) Evolution of band structures of $(\text{Cs}_4\text{CuBiI}_8)_1/(\text{Cs}_4\text{AgInI}_8)_5$, $(\text{Cs}_4\text{CuBiI}_8)_2/(\text{Cs}_4\text{AgInI}_8)_4$, $(\text{Cs}_4\text{CuBiI}_8)_4/(\text{Cs}_4\text{AgInI}_8)_2$, and $(\text{Cs}_4\text{CuBiI}_8)_5/(\text{Cs}_4\text{AgInI}_8)_1$ LHs. For simplicity, we label the corresponding indices (m, n) here. All bands are shifted to align the deep Cs $5s$ states. The inset shows the charge density corresponding to the state VB1. The values of valence band splitting between VB1 and VB2 at the Γ point are given in the band structures for all direct band gap LHs. Transition dipole matrix elements between band edges for (b) $(\text{Cs}_4\text{CuBiI}_8)_4/(\text{Cs}_4\text{AgInI}_8)_2$ and (c) $(\text{Cs}_4\text{CuBiI}_8)_5/(\text{Cs}_4\text{AgInI}_8)_1$ LHs. (d) Electron and hole effective mass for $(\text{Cs}_4\text{CuBiI}_8)_m/(\text{Cs}_4\text{AgInI}_8)_n$ LHs.

semiconducting nature in all considered $(\text{Cs}_4\text{CuBiI}_8)_m/(\text{Cs}_4\text{AgInI}_8)_n$ LHs are maintained, with similar band gap $\sim 0.80 \text{ eV}$, as presented in Table 1. This is very different from the cases of As_m/Sb_n heterostructures,²⁵ whose band gap and band nature depend on the building block width. When m is smaller than 3, $(\text{Cs}_4\text{CuBiI}_8)_m/(\text{Cs}_4\text{AgInI}_8)_n$ LHs show an undesired indirect-gap feature. For $(\text{Cs}_4\text{CuBiI}_8)_2/(\text{Cs}_4\text{AgInI}_8)_4$, i.e. (2, 4), the indirect band dispersion is similar to that of monolayer InSe,⁴⁶ especially with the similar Mexican hat valence band of 15 meV . For the cases of $m \geq 3$, the VB at Γ point shifts toward the Fermi level, leading to an intriguing indirect-to-direct band gap transition. Moreover, the VBM is mainly derived from the Cu d_z^2 and I p orbitals in the inset of Figure 5a, and the values of valence band splitting at the Γ point decreasing from 0.29 to 0.12 eV , when m increases from 3 to 5. The reduced valence band splitting indicates that the interaction between VB1 and VB2 is weakened by the

length of the $\text{Cs}_4\text{CuBiI}_8$ constituent. On the basis of the discussions above, we have demonstrated that the $(\text{Cs}_4\text{CuBiI}_8)_m/(\text{Cs}_4\text{AgInI}_8)_n$ LHs can possess the direct band gap only if the condition of $m \geq 3$ is satisfied. For application in optoelectronic devices, $(\text{Cs}_4\text{CuBiI}_8)_m/(\text{Cs}_4\text{AgInI}_8)_n$ LHs should follow this criteria to ensure the integral light emission efficiency.

Next, we focus on the cases of $m \geq 3$ to discuss the carrier effective mass in Figure 5d, which is crucial for optoelectronic application. It is found that the hole effective mass, dominated by the $\text{Cs}_4\text{CuBiI}_8$ component, decreases significantly with the increasing m value. For example, the hole effective mass is $0.76 m_0$ for (5, 1) LH along the Γ -X direction, much smaller than the heavy hole for (3, 3) LH ($7.63 m_0$). This means that the hole mobility can be enhanced substantially. However, the electron effective mass, contributed by the $\text{Cs}_4\text{AgInI}_8$ component, shows the opposite tendency, increasing with the increasing m value. At this point, the feature of carrier effective mass becomes apparent, i.e., both the electron and hole effective mass of $(\text{Cs}_4\text{CuBiI}_8)_m/(\text{Cs}_4\text{AgInI}_8)_n$ decrease with larger m and n . This can be verified by much smaller effective electron and hole masses in $(\text{Cs}_4\text{CuBiI}_8)_4/(\text{Cs}_4\text{AgInI}_8)_4$ LH, which are 0.36 (0.35) and 0.45 (0.51) m_0 along the Γ -X (Γ -M) direction (see Table 1). Therefore, high charge carrier mobility can be realized in the seamless $(\text{Cs}_4\text{CuBiI}_8)_m/(\text{Cs}_4\text{AgInI}_8)_n$ LHs by enlarging the width m and n values.

We also investigate the transition dipole matrix elements (P^2) between band edges for $(\text{Cs}_4\text{CuBiI}_8)_m/(\text{Cs}_4\text{AgInI}_8)_n$ ($m > 3$) LHs with direct gaps and focus on the P^2 value at Γ point in Figure 5b,c. Fortunately, the P^2 value can be modified by the component length. For example, the $(\text{Cs}_4\text{CuBiI}_8)_4/(\text{Cs}_4\text{AgInI}_8)_2$ and $(\text{Cs}_4\text{CuBiI}_8)_5/(\text{Cs}_4\text{AgInI}_8)_1$ LHs have considerable P^2 between the band edges at Γ point, which is beneficial for the solar absorption. Compared with the partially forbidden transitions at the Γ point for $(\text{Cs}_4\text{CuBiI}_8)_3/(\text{Cs}_4\text{AgInI}_8)_3$ LH, the optical transitions in $(\text{Cs}_4\text{CuBiI}_8)_m/(\text{Cs}_4\text{AgInI}_8)_n$ ($m > n$) are allowed. This is another criterion to design suitable $(\text{Cs}_4\text{CuBiI}_8)_m/(\text{Cs}_4\text{AgInI}_8)_n$ LHs for solar cell applications.

For the practical fabrication and device applications, it is important to study the mechanical properties of halide perovskites. In the last part of our Letter, we take $(\text{Cs}_4\text{CuBiI}_8)_3/(\text{Cs}_4\text{AgInI}_8)_3$ LH as an example to study the mechanical properties of these 2D LHs. The calculated elastic constants of this component are $C_{11} = 15.70$, $C_{22} = 14.53$, $C_{12} = 4.08$, and $C_{66} = 9.60$ N/m (for details see Table S4), which satisfy the Born criteria $C_{11}C_{22} - C_{12}^2 > 0$ and $C_{66} > 0$. Hence, the seamless $(\text{Cs}_4\text{CuBiI}_8)_3/(\text{Cs}_4\text{AgInI}_8)_3$ LH is mechanically stable, in line with the previous results of binding energy analysis. The derived Young's modulus (~ 14 N/m) and shear modulus (~ 10 N/m) in lateral heterostructures indicate that its stiffness is much smaller than that of monolayer graphene (340 N/m) and borophene (380 N/m).⁴⁷ The Young's modulus is also smaller than that of the monolayer $(\text{CH}_3(\text{CH}_2)_2\text{NH}_3)_2(\text{CH}_3\text{-NH}_3)_2\text{Pb}_3\text{I}_{10}$ (29.4 ± 3.6 N/m).⁴⁸ This difference may mainly result from the effect of A-site cation. The Poisson's ratio (~ 0.27) is greater than that of graphene (0.18) and borophene (0.02).⁴⁷ Therefore, $(\text{Cs}_4\text{CuBiI}_8)_3/(\text{Cs}_4\text{AgInI}_8)_3$ LH is more flexible than graphene, similar to other typical inorganic halide perovskites. This is attributed to the soft metal-halide bond in halide perovskites compared to those covalently bonded 2D materials.¹³

Furthermore, the directional Young's modulus $Y_{2D}(\theta)$ and Poisson's ratio $\nu_{2D}(\theta)$ of $(\text{Cs}_4\text{CuBiI}_8)_3/(\text{Cs}_4\text{AgInI}_8)_3$ LH are displayed in Figure 6. It is shown that $(\text{Cs}_4\text{CuBiI}_8)_3/$

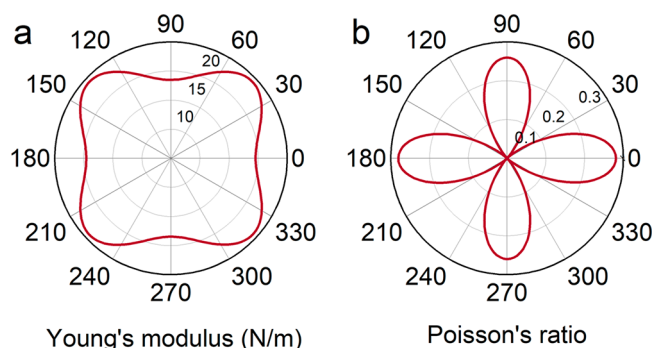


Figure 6. Orientational-dependence of (a) Young's modulus and (b) Poisson's ratio of $(\text{Cs}_4\text{CuBiI}_8)_3/(\text{Cs}_4\text{AgInI}_8)_3$ LH.

$(\text{Cs}_4\text{AgInI}_8)_3$ LH exhibits anisotropic Young's modulus and Poisson's ratios with a clear angle-dependent feature. The minimum (maximum) Young's modulus (Poisson's ratio) is 13.47 (0.28) along the direction of $0^\circ, 90^\circ, 180^\circ,$ and 270° , and the maximum (minimum) Young's modulus (Poisson's ratio) is 19.21 (0.00) along the direction of $45^\circ, 135^\circ, 225^\circ,$ and 315° . In fact, the nature of anisotropic mechanical properties can be explained by analyzing the distribution of charge densities.⁴⁹ The charge densities of $(\text{Cs}_4\text{CuBiI}_8)_3/(\text{Cs}_4\text{AgInI}_8)_3$ LH are not uniformly distributed but form patterns continuing along the diagonal direction in Figure S11. This is, indeed, consistent with the calculated Young's modulus, in which the maximum values appear in a continuous pattern. The electron orbitals are hybridized more strongly along these directions, leading to a larger overlap of wave functions and stronger bonding strength, and subsequently higher stiffness. On the other hand, the charge densities of $(\text{Cs}_4\text{CuBiI}_8)_3/(\text{Cs}_4\text{AgInI}_8)_3$ LH have the lowest value along the x and y directions, resulting in the minimum values of Young's modulus. The anisotropic mechanical properties in $(\text{Cs}_4\text{CuBiI}_8)_3/(\text{Cs}_4\text{AgInI}_8)_3$ LH make it useful in the field of special flexible electronic devices.

In summary, we have investigated the electronic, optical, and mechanical properties of $(\text{Cs}_4\text{CuBiI}_8)_m/(\text{Cs}_4\text{AgInI}_8)_n$ LHs using first-principles calculations. Our results reveal that $(\text{Cs}_4\text{CuBiI}_8)_3/(\text{Cs}_4\text{AgInI}_8)_3$ LH has favored direct band gap and type-II alignment, but with undesired heavy hole and partially forbidden transition between band edges. Fortunately, the undesired properties can be modulated effectively by applying strain or changing the block size. The hole effective mass can be reduced by 1 order of magnitude via tensile strain or enlarging the block size of the $\text{Cs}_4\text{CuBiI}_8$ component. The partially forbidden transitions can also be tuned by applying strain or adjusting components in perovskites. For the mechanical properties of $(\text{Cs}_4\text{CuBiI}_8)_3/(\text{Cs}_4\text{AgInI}_8)_3$ LH, the calculated Young's modulus and Poisson's ratios are both anisotropic, and its mechanical flexibility is comparable to typical double perovskites. Our studies provide possible structures for experimentally achieving double perovskite LHs with tunable optoelectronic properties. Furthermore, we note that the conjugated organic ligands are the critical points to realize monolayer halide double perovskites in experiments. The role of the long-chain organic molecule on the chemical stability and optoelectronic properties of the lateral hetero-

structures thus deserves deeper attention. On the other hand, there are two kinds of halide double perovskites structures, i.e., Ruddlesden–Popper (near Dion–Jacobson) and Dion–Jacobson. It is also interesting to investigate the interfacial properties of Dion–Jacobson halide double perovskite lateral heterostructures.

During the revision of our manuscript, we became aware of a related joint experiment–theory study by Dou et al.,³⁰ which demonstrated the epitaxial growth of atomically sharp lateral heterostructures of 2D halide perovskites. Their study reported the modulation of the optical and electronic properties of 2D halide perovskite heterostructures by varying the inorganic composition and demonstrated the possibility of tuning the optoelectronic properties via lattice-strain engineering at the interfaces of the heterostructures. In our theoretical work, we revealed that the optoelectronic properties of lateral heterostructures of monolayer halide double perovskites can be effectively modified by applying epitaxial strain or adjusting inorganic components, in good agreement with this experimental work.

■ ASSOCIATED CONTENT

Supporting Information

The Supporting Information is available free of charge at <https://pubs.acs.org/doi/10.1021/acsenerylett.0c01046>.

Calculation method, optimized lattice constant, bond length, atomic position, band structure, band gap, PDOS, electron localization functions, transition dipole moments, distribution of charge density, estimated electron populations, and summary of the calculated mechanical parameters (PDF)

■ AUTHOR INFORMATION

Corresponding Authors

Gang Tang – *Theoretical Materials Physics, Q-MAT, CESAM, University of Liège, B-4000 Liège, Belgium*; Email: gtang@uliege.be

Shengjun Yuan – *School of Physics and Technology, Wuhan University, Wuhan 430072, People's Republic of China*; Email: s.yuan@whu.edu.cn

Authors

Hongxia Zhong – *School of Physics and Technology, Wuhan University, Wuhan 430072, People's Republic of China*

Mao Yang – *Institut für Physik and IRIS Adlershof, Humboldt-Universität zu Berlin, Berlin 12489, Germany; School of Science, Xi'an Polytechnic University, Xi'an 710048, P.R. China*; orcid.org/0000-0003-1488-4671

Complete contact information is available at:

<https://pubs.acs.org/doi/10.1021/acsenerylett.0c01046>

Notes

The authors declare no competing financial interest.

■ ACKNOWLEDGMENTS

This work is supported by the National Natural Science Foundation of China (Grant Nos. 11947218, 11547256, and 11704300). H.Z. acknowledges the support by the China Postdoctoral Science Foundation (Grant No. 2018M640723). Numerical calculations presented in this Letter were performed on a supercomputing system in the Supercomputing Center of Wuhan University.

■ REFERENCES

- (1) Jiang, Q.; Zhao, Y.; Zhang, X.; Yang, X.; Chen, Y.; Chu, Z.; Ye, Q.; Li, X.; Yin, Z.; You, J. Surface passivation of perovskite film for efficient solar cells. *Nat. Photonics* **2019**, *13* (7), 460–466.
- (2) Tsai, H.; Nie, W.; Blancon, J.-C.; Stoumpos, C. C.; Asadpour, R.; Harutyunyan, B.; Neukirch, A. J.; Verduzco, R.; Crochet, J. J.; Tretiak, S.; et al. High-efficiency two-dimensional Ruddlesden–Popper perovskite solar cells. *Nature* **2016**, *536* (7616), 312–316.
- (3) Ling, Y.; Yuan, Z.; Tian, Y.; Wang, X.; Wang, J. C.; Xin, Y.; Hanson, K.; Ma, B.; Gao, H. Bright light-emitting diodes based on organometal halide perovskite nanoplatelets. *Adv. Mater.* **2016**, *28* (2), 305–311.
- (4) Zhu, H.; Fu, Y.; Meng, F.; Wu, X.; Gong, Z.; Ding, Q.; Gustafsson, M. V.; Trinh, M. T.; Jin, S.; Zhu, X. Lead halide perovskite nanowire lasers with low lasing thresholds and high quality factors. *Nat. Mater.* **2015**, *14* (6), 636–642.
- (5) Ahmadi, M.; Wu, T.; Hu, B. A review on organic–inorganic halide perovskite photodetectors: device engineering and fundamental physics. *Adv. Mater.* **2017**, *29* (41), 1605242.
- (6) Babayigit, A.; Ethirajan, A.; Muller, M.; Conings, B. Toxicity of organometal halide perovskite solar cells. *Nat. Mater.* **2016**, *15* (3), 247.
- (7) Luo, J.; Wang, X.; Li, S.; Liu, J.; Guo, Y.; Niu, G.; Yao, L.; Fu, Y.; Gao, L.; Dong, Q.; et al. Efficient and stable emission of warm-white light from lead-free halide double perovskites. *Nature* **2018**, *563* (7732), 541–545.
- (8) Pan, W.; Wu, H.; Luo, J.; Deng, Z.; Ge, C.; Chen, C.; Jiang, X.; Yin, W.-J.; Niu, G.; Zhu, L. Cs₂AgBiBr₆ single-crystal X-ray detectors with a low detection limit. *Nat. Photonics* **2017**, *11* (11), 726–732.
- (9) Meng, W.; Wang, X.; Xiao, Z.; Wang, J.; Mitzi, D. B.; Yan, Y. Parity-forbidden transitions and their impact on the optical absorption properties of lead-free metal halide perovskites and double perovskites. *J. Phys. Chem. Lett.* **2017**, *8* (13), 2999–3007.
- (10) Slavney, A. H.; Leppert, L.; Bartesaghi, D.; Gold-Parker, A.; Toney, M. F.; Savenije, T. J.; Neaton, J. B.; Karunadasa, H. I. Defect-induced band-edge reconstruction of a bismuth-halide double perovskite for visible-light absorption. *J. Am. Chem. Soc.* **2017**, *139* (14), 5015–5018.
- (11) Xiao, Z.; Du, K.-Z.; Meng, W.; Wang, J.; Mitzi, D. B.; Yan, Y. Intrinsic instability of Cs₂In(I)M(III)X₆ (M = Bi, Sb; X = halogen) double perovskites: a combined density functional theory and experimental study. *J. Am. Chem. Soc.* **2017**, *139* (17), 6054–6057.
- (12) Zhao, X.-G.; Yang, J.-H.; Fu, Y.; Yang, D.; Xu, Q.; Yu, L.; Wei, S.-H.; Zhang, L. Design of lead-free inorganic halide perovskites for solar cells via cation-transmutation. *J. Am. Chem. Soc.* **2017**, *139* (7), 2630–2638.
- (13) Tang, G.; Xiao, Z.; Hong, J. Designing two-dimensional properties in three-dimensional halide perovskites via orbital engineering. *J. Phys. Chem. Lett.* **2019**, *10* (21), 6688–6694.
- (14) Savory, C. N.; Walsh, A.; Scanlon, D. O. Can Pb-Free halide double perovskites support high-efficiency solar cells? *ACS Energy Lett.* **2016**, *1* (5), 949–955.
- (15) Connor, B. A.; Leppert, L.; Smith, M. D.; Neaton, J. B.; Karunadasa, H. I. Layered halide double perovskites: dimensional reduction of Cs₂AgBiBr₆. *J. Am. Chem. Soc.* **2018**, *140* (15), 5235–5240.
- (16) Jana, M. K.; Janke, S. M.; Dirkes, D. J.; Dovletgeldi, S.; Liu, C.; Qin, X.; Gundogdu, K.; You, W.; Blum, V.; Mitzi, D. B. Direct-Bandgap 2D silver–bismuth iodide double perovskite: the structure-directing influence of an oligothiophene spacer cation. *J. Am. Chem. Soc.* **2019**, *141* (19), 7955–7964.
- (17) Bi, L.-Y.; Hu, Y.-Q.; Li, M.-Q.; Hu, T.-L.; Zhang, H.-L.; Yin, X.-T.; Que, W.-X.; Lassoued, M. S.; Zheng, Y.-Z. Two-dimensional lead-free iodide-based hybrid double perovskites: crystal growth, thin-film preparation and photocurrent responses. *J. Mater. Chem. A* **2019**, *7* (34), 19662–19667.
- (18) Mao, L.; Teicher, S. M.; Stoumpos, C. C.; Kennard, R. M.; DeCrescent, R. A.; Wu, G.; Schuller, J. A.; Chabinc, M. L.; Cheetham, A. K.; Seshadri, R. Chemical and structural diversity of

hybrid layered double perovskite halides. *J. Am. Chem. Soc.* **2019**, *141* (48), 19099–19109.

(19) Tang, G.; Xiao, Z.; Hosono, H.; Kamiya, T.; Fang, D.; Hong, J. Layered halide double perovskites $\text{Cs}_{3+n}\text{M}(\text{II})_n\text{Sb}_2\text{X}_{9+3n}$ (M = Sn, Ge) for photovoltaic applications. *J. Phys. Chem. Lett.* **2018**, *9* (1), 43–48.

(20) Cheng, H.-C.; Wang, G.; Li, D.; He, Q.; Yin, A.; Liu, Y.; Wu, H.; Ding, M.; Huang, Y.; Duan, X. Van der Waals heterojunction devices based on organohalide perovskites and two-dimensional materials. *Nano Lett.* **2016**, *16* (1), 367–373.

(21) Guo, Y.; Saidi, W. A.; Wang, Q. 2D halide perovskite-based van der Waals heterostructures: contact evaluation and performance modulation. *2D Mater.* **2017**, *4* (3), No. 035009.

(22) Shi, E.; Gao, Y.; Finkenauer, B. P.; Coffey, A. H.; Dou, L. Two-dimensional halide perovskite nanomaterials and heterostructures. *Chem. Soc. Rev.* **2018**, *47* (16), 6046–6072.

(23) Wang, J.; Li, J.; Tan, Q.; Li, L.; Zhang, J.; Zang, J.; Tan, P.; Zhang, J.; Li, D. Controllable synthesis of two-dimensional Ruddlesden–Popper-type perovskite heterostructures. *J. Phys. Chem. Lett.* **2017**, *8* (24), 6211–6219.

(24) Gong, Y.; Lin, J.; Wang, X.; Shi, G.; Lei, S.; Lin, Z.; Zou, X.; Ye, G.; Vajtai, R.; Yakobson, B. I.; et al. Vertical and in-plane heterostructures from WS_2/MoS_2 monolayers. *Nat. Mater.* **2014**, *13* (12), 1135–1142.

(25) Sun, Q.; Dai, Y.; Ma, Y.; Yin, N.; Wei, W.; Yu, L.; Huang, B. Design of lateral heterostructure from arsenene and antimonene. *2D Mater.* **2016**, *3* (3), No. 035017.

(26) Sahoo, P. K.; Memaran, S.; Xin, Y.; Balicas, L.; Gutiérrez, H. R. One-pot growth of two-dimensional lateral heterostructures via sequential edge-epitaxy. *Nature* **2018**, *553* (7686), 63–67.

(27) Hwang, B.; Lee, J. S. 2D perovskite-based self-aligned lateral heterostructure photodetectors utilizing vapor deposition. *Adv. Opt. Mater.* **2019**, *7* (3), 1801356.

(28) Kennard, R. M.; Dahlman, C. J.; Nakayama, H.; DeCrescent, R. A.; Schuller, J. A.; Seshadri, R.; Mukherjee, K.; Chabinyk, M. L. Phase stability and diffusion in lateral heterostructures of methyl ammonium lead halide perovskites. *ACS Appl. Mater. Interfaces* **2019**, *11* (28), 25313–25321.

(29) Wang, Y.; Chen, Z.; Deschler, F.; Sun, X.; Lu, T.-M.; Wertz, E. A.; Hu, J.-M.; Shi, J. Epitaxial halide perovskite lateral double heterostructure. *ACS Nano* **2017**, *11* (3), 3355–3364.

(30) Shi, E.; Yuan, B.; Shiring, S. B.; Gao, Y.; Guo, Y.; Su, C.; Lai, M.; Yang, P.; Kong, J.; Savoie, B. M. Two-dimensional halide perovskite lateral epitaxial heterostructures. *Nature* **2020**, *580* (7805), 614–620.

(31) Tremblay, M.-H. I. n.; Bacsá, J.; Zhao, B.; Pulvirenti, F.; Barlow, S.; Marder, S. R. Structures of $(4\text{-Y-C}_6\text{H}_4\text{CH}_2\text{NH}_3)_2\text{PbI}_4$ {Y = H, F, Cl, Br, I}: Tuning of Hybrid Organic Inorganic Perovskite Structures from Ruddlesden–Popper to Dion–Jacobson Limits. *Chem. Mater.* **2019**, *31* (16), 6145–6153.

(32) Xiao, Z.; Meng, W.; Wang, J.; Mitzi, D. B.; Yan, Y. Searching for promising new perovskite-based photovoltaic absorbers: The importance of electronic dimensionality. *Mater. Horiz.* **2017**, *4*, 206–216.

(33) Tang, G.; Hong, J. Direct tuning of the band gap via electronically-active organic cations and large piezoelectric response in one-dimensional hybrid halides from first-principles. *J. Mater. Chem. C* **2018**, *6* (28), 7671–7676.

(34) Zhao, X.-G.; Yang, D.; Sun, Y.; Li, T.; Zhang, L.; Yu, L.; Zunger, A. Cu-In Halide Perovskite (CIHP) solar absorbers. *J. Am. Chem. Soc.* **2017**, *139* (19), 6718.

(35) Feng, H. J.; Deng, W.; Yang, K.; Huang, J.; Zeng, X. C. Double Perovskite Cs_2BBiX_6 (B = Ag, Cu; X = Br, Cl)/ TiO_2 Heterojunction: An Efficient Pb-Free Perovskite Interface for Charge Extraction. *J. Phys. Chem. C* **2017**, *121* (8), 4471.

(36) Wang, V.; Xu, N.; Liu, J. C.; Tang, G.; Geng, W.-T. VASPKIT: A Pre- and Post-Processing Program for VASP code. *arXiv* **2020**, 1908.08269.

(37) Yuan, J.; Yu, N.; Wang, J.; Xue, K. H.; Miao, X. Design lateral heterostructure of monolayer ZrS_2 and HfS_2 from first principles calculations. *Appl. Surf. Sci.* **2018**, *436*, 919–926.

(38) Milina, M.; Mitchell, S.; Cooke, D.; Crivelli, P.; Pérez-Ramírez, J. Impact of pore connectivity on the design of long-lived zeolite catalysts. *Angew. Chem., Int. Ed.* **2015**, *54* (5), 1678–1678.

(39) Kaiukov, R.; Almeida, G.; Marras, S.; Dang, Z.; Baranov, D.; Petralanda, U.; Infante, I.; Mugnaioli, E.; Griesi, A.; De Trizio, L.; et al. $\text{Cs}_3\text{Cu}_4\text{In}_2\text{Cl}_{13}$ nanocrystals: A perovskite-related structure with inorganic clusters at A Sites. *Inorg. Chem.* **2020**, *59* (1), 548–554.

(40) Debbichi, L.; Lee, S.; Cho, H.; Rappe, A. M.; Hong, K. H.; Jang, M. S.; Kim, H. Mixed Valence Perovskite $\text{Cs}_2\text{Au}_2\text{I}_6$: A Potential Material for Thin-Film Pb-Free Photovoltaic Cells with Ultrahigh Efficiency. *Adv. Mater.* **2018**, *30* (12), 1707001.

(41) Giorgi, G.; Yamashita, K.; Palumbo, M. Two-dimensional optical excitations in the mixed-valence $\text{Cs}_2\text{Au}_2\text{I}_6$ fully inorganic double perovskite. *J. Mater. Chem. C* **2018**, *6* (38), 10197–10201.

(42) Yin, W. J.; Shi, T.; Yan, Y. Superior photovoltaic properties of lead halide perovskites: insights from first-principles theory. *J. Phys. Chem. C* **2015**, *119* (10), 5253–5264.

(43) Steele, J. A.; Jin, H.; Dovgaliuk, I.; Berger, R. F.; Braeckvelt, T.; Yuan, H.; Martin, C.; Solano, E.; Lejaeghere, K.; Rogge, S. M.; et al. Thermal nonequilibrium of strained black CsPbI_3 thin films. *Science* **2019**, *365* (6454), 679–684.

(44) Tsai, H.; Asadpour, R.; Blancon, J. C.; Stoumpos, C. C.; Durand, O.; Strzalka, J. W.; Chen, B.; Verduzco, R.; Ajayan, P. M.; Tretiak, S.; et al. Light-induced lattice expansion leads to high-efficiency perovskite solar cells. *Science* **2018**, *360* (6384), 67–70.

(45) Zheng, F.; Tan, L. Z.; Liu, S.; Rappe, A. M. Rashba spin–orbit coupling enhanced carrier lifetime in $\text{CH}_3\text{NH}_3\text{PbI}_3$. *Nano Lett.* **2015**, *15* (12), 7794–7800.

(46) Lugovskoi, A.; Katsnelson, M.; Rudenko, A. Strong electron-phonon coupling and its influence on the transport and optical properties of hole-doped single-layer InSe. *Phys. Rev. Lett.* **2019**, *123* (17), 176401.

(47) Zhong, H.; Huang, K.; Yu, G.; Yuan, S. Electronic and mechanical properties of few-layer borophene. *Phys. Rev. B: Condens. Matter Phys.* **2018**, *98* (5), No. 054104.

(48) Tu, Q.; Spanopoulos, I.; Yasaei, P.; Stoumpos, C. C.; Kanatzidis, M. G.; Shekhawat, G. S.; Dravid, V. P. Stretching and breaking of ultrathin 2D hybrid organic–inorganic perovskites. *ACS Nano* **2018**, *12* (10), 10347–10354.

(49) Xiong, W.; Huang, K.; Yuan, S. The mechanical, electronic and optical properties of two-dimensional transition metal chalcogenides MX_2 and M_2X_3 (M = Ni, Pd; X = S, Se, Te) with hexagonal and orthorhombic structures. *J. Mater. Chem. C* **2019**, *7* (43), 13518.